Plasmon coupling in topological insulator multilayers

Zhengtianye Wang, Theresa P. Ginley, Sivakumar Vishnuvardhan Mambakkam, Greeshma Chandan,
Yuying Zhang, Chaoying Ni, and Stephanie Law*
Department of Materials Science and Engineering, University of Delaware, Newark Delaware 19716, USA

(Received 20 July 2020; accepted 19 October 2020; published 9 November 2020)

Topological insulators (TIs) house two-dimensional Dirac plasmons on their surfaces. In TI thin films, plasmons on the top and bottom surfaces couple electrostatically, giving rise to an acoustic and an optical plasmon mode. By extension, a superlattice comprising TI layers and trivially insulating layers could house multiple complex plasmon modes which could be used to create a new type of Dirac metamaterial. In this paper, we synthesize TI superlattices, fabricate them into stripe arrays, characterize their optical and plasmonic properties, and model the samples using transfer matrices. We excite plasmon modes that couple to the phonons in the superlattice, resulting in hybrid plasmon-phonon polaritons. These modes are modeled using an analytical Fano resonance model and the extracted resonant positions are reproduced by transfer matrix modeling. We also excite an epsilon near-zero mode in the top dielectric material $(Bi_{0.5}In_{0.5})_2Se_3$. Understanding the behavior of the polariton modes in this complex system will lend insight into the many-body interaction in low-dimensional systems.

DOI: 10.1103/PhysRevMaterials.4.115202

I. INTRODUCTION

Layered van der Waals materials like Bi_2Se_3, Bi_2Te_3, and Sb_2Te_3 have been rediscovered as topological insulators (TIs) in the past decade [1]. Due to the large spin-orbit coupling arising from heavy elements like bismuth and antimony, these materials exhibit an inverted band structure which causes the formation of nontrivial topological surface states (TSS). The TSS form a Dirac cone within the bulk band gap at a high-symmetry point in the Brillouin zone. The electrons occupying the TSS exhibit spin-momentum locking, which prevents them from backscattering into other surface states in the absence of a magnetic perturbation. Such inherent robustness makes the TSS more resistant to surface quality issues and ensures a longer lifetime of processes leveraging the TSS. Electrons occupying the TSS are massless Dirac fermions, characterized by a linear energy/momentum dispersion and vanishing density of states near the Dirac point. The unique properties of the TSS have great promise in tunable THz detectors [2–4] and emitters [5], quantum computing [6], and spintronic devices [7,8]. In addition to these and other applications, the TSS can also house two-dimensional (2D) spin-polarized Dirac plasmons. These plasmons are of interest both for their unusual physics as well as their optoelectronic device applications in the THz spectral range [9]. In this paper, we will investigate the coupling among TI Dirac plasmon polaritons in multilayer heterostructures through both transfer matrix method (TMM) modeling and experiment to understand how the coupling depends on the physical parameters of the system including layer thicknesses and wave vector.

The behavior of TI Dirac plasmons is not dissimilar to that of the more well-studied graphene plasmons. Both materials show a Dirac cone band structure, which leads to plasmons in which $\omega \propto n^{1/4}$ where ω is the plasmon frequency and n is the 2D carrier density. In general, the plasmon resonances in Dirac fermion systems are in the midinfrared and terahertz bands; these frequency ranges have many applications which would benefit from plasmonic devices [9,10]. For example, both materials are highly sensitive to changes in the surrounding dielectric, making them promising for applications in on-chip sensors. However, unlike graphene, plasmons arising from the TSS are also predicted to carry a spin-density wave [11], as a result of strong spin-orbit coupling inside the bulk. TIs are the only known example of a single-material system that can house a spin plasmon. Another thing that distinguishes TI thin-film plasmons from graphene is their morphology. It is easy to grow TI thin films at a wafer scale, which makes device patterning straightforward. Finally, unlike graphene which is by nature a single layer, TI thin films with thicknesses above the critical thickness will always house coupled Dirac plasmons, since plasmons will be excited on the top and bottom surfaces simultaneously. This leads to a bonding and an antibonding mode, or alternatively, an acoustic and an optical plasmon mode.

There have been significant previous efforts investigating the physics of Dirac plasmons in single-layer TIs. Dirac plasmons in Bi_2Se_3 were first optically probed experimentally by Di Pietro *et al.* and a square-root $\omega(q_\parallel)$ dispersion relationship was reported where $q_\parallel$ is the in-plane momentum [12]. This type of dispersion relationship is characteristic of 2D plasmons. Plasmons can also be excited and probed by electronic spectroscopy, for example, electron energy-loss spectroscopy (EELS). EELS measurements demonstrated that the morphology of the Bi_2Se_3 surface plays a crucial role in determining

---

*slaw@udel.edu

the dominant plasmon type in excitations [13]. Samples prepared by blade cleaving show large flat terraces leading to excitation of Dirac plasmons and 2D electron gas (2DEG) surface plasmons [14], which can be further distinguished by mapping out their dispersions respectively. On the contrary, samples prepared by exfoliation show significant surface roughness and large quantity of defects, thus leading to the excitation of plasmons arising from massive bulk electrons [15]. Ginley and Law studied how the plasmon frequency depends on the Bi_2Se_3 film thickness and showed conclusively that the plasmon excitations in the THz range arise mainly from the TSS electrons [16]. TI plasmons have also been investigated in other chalcogenide compounds like Bi_2Te_3 [17] and $Bi_{1.5}Sb_{0.5}Te_{1.8}Se_{1.2}$ alloys [18] in the visible range. In addition, plasmons in a microring geometry were also studied, where bonding/antibonding plasmon modes formed due to plasmon hybridization [19]. Finally, because the bulk dielectric constant of TI materials is large (∼20–100, depending on measurement technique) [20,21], these coupled plasmons show extremely large mode indices which may be useful in future on-chip THz applications.

Despite these significant achievements, to date there have been few investigations of the physics of TI plasmons in multilayer heterostructures. In traditional materials, it is known that plasmons can couple across multiple interfaces in metal/dielectric heterostructures. This leads to complex bulk plasmon modes and, with enough layers, to hyperbolic metamaterial behavior in normal metal/dielectric heterostructures [22,23]. In a material hosting Dirac plasmons like graphene or TIs, we would expect to observe similar complex coupled plasmon modes, with the potential to create a Dirac metamaterial. There is existing work on related graphene/dielectric plasmonic multilayer structures [10,24–29]. Nevertheless, experimental research into the plasmonic excitations of graphene multilayer structures has been relatively limited. This is likely due to the difficulty in fabricating these structures: structures are usually made by transferring one graphene layer onto a substrate, depositing a dielectric spacer, transferring the next graphene layer, and so on. Direct growth of graphene multilayer heterostructures is still challenging, making it difficult to understand the properties of plasmon modes in stacked graphene structures, which is essential for creating Dirac metamaterials.

Fortunately, we can create large-area films containing multiple coupled Dirac plasmons by growing TI/band insulator (BI) heterostructure using well-developed semiconductor thin-film techniques like molecular-beam epitaxy (MBE). Compared to stacking graphene layers and dielectrics using transfer techniques, the growth of chalcogenide materials via MBE is straightforward, controllable, and wafer scale. This allows us to study plasmon coupling across band insulators and plasmon coupling across multiple TI interfaces. Due to the unique properties of the TSS electrons in TIs, the collective modes in these layered structures are likely to have exotic optical and spin properties.

Superlattices of TI/BI materials have been grown previously using BI materials like ZnSe [30], $Zn_xCd_{1-x}Se$ [31], and In_2Se_3 [32,33]. In our heterostructure of alternating TI/BI layers, we use $(Bi_{0.5}In_{0.5})_2Se_3$ (BIS) as the BI material. Both Bi_2Se_3 and BIS can be synthesized via MBE using a selenium cracker source [34,35]. BIS is preferred over pure In_2Se_3 due to its closer lattice match to Bi_2Se_3 and the reduction of indium diffusion into the TI layer [36]. For indium concentrations above $x = 0.06$, $(Bi_{1-x}In_x)_2Se_3$ is a topologically trivial material [37]. Topological surface states are thus expected at each Bi_2Se_3 and BIS interface.

In this paper, we model, fabricate, and characterize multilayer TI/BI structures and examine their structural and optical properties. This paper will be divided into four parts: In Sec. II, we will introduce the analytical form of the coupled plasmon dispersion in a single-layer TI and the optical properties of $(Bi_{0.5}In_{0.5})_2Se_3$. In Sec. III, we develop and validate a TMM to investigate the optical properties of coupled plasmon modes in a single layer of Bi_2Se_3. Finally, in Sec. IV we fabricate structures comprising three BIS layers and two Bi_2Se_3 layers and measure the extinction of the films as a function of wave vector to probe the polariton dispersion experimentally. We change both the central BI spacer layer thickness as well as the TI layer thicknesses to understand Dirac plasmon coupling. Plasmon-phonon polariton modes are observed in all samples. The experimental results are compared to TMM modeling with good agreement, and Dirac plasmon coupling across band insulator is confirmed. These results are a step toward creating a TI-based Dirac metamaterial.

II. ANALYTICAL FORM OF DIRAC PLASMON DISPERSION AND MATERIAL PERMITTIVITIES

Before we can explore plasmon coupling in a TI multilayer heterostructure, we must first understand the behavior of plasmons in single TI layers. The Dirac plasmons in TIs are similar to the graphene/dielectric/graphene (G/D/G) structure: they are both Dirac fermion systems, they are two dimensional, the Dirac fermion layers are coupled to each other across a dielectric (the bulk material in the TI case), and the long range Coulomb electron interactions are non-negligible. Therefore, it is common to model plasmons in thin TI films using formalism developed for the coupled G/D/G system. Dirac plasmon coupling in a G/D/G structure in which the dielectric layer is thin relative to the wavelength of light has been studied extensively [25,38–41]. If we only consider the electrostatic interaction, ignore the tunneling of carriers, and apply the long-wavelength limit $q \ll k_F$ where q is the plasmon wave vector and k_F is the Fermi wave vector of the graphene or the TSS electrons, the hybridization of the top and bottom plasmons generates an optical mode and an acoustic mode. For this formalism to apply, the TI film must be thinner than the TSS plasmon decay length in the bulk (∼1 μm), and the TI film must be thicker than the critical thickness for the quantum tunneling of surface states (∼6–8 nm) [42,43]. Even though TI thin films and G/D/G systems are similar, we still note several unique features of TI: the strong spin-orbit coupling inside the TI bulk leads to opposite Fermi velocities for the top and bottom surfaces (spin degeneracy $g_s = 1$), a spin wave is predicted to accompany the plasmon charge-density wave due to the spin-momentum locking, and a single Dirac cone resides at the high-symmetry Γ point in the TI Brillouin zone (valley degeneracy $g_v = 1$) as compared to the two Dirac cones at the K and K' points in the graphene Brillouin zone ($g_v = 2$). For the purposes of this paper, we will set aside the spin-momentum locking and focus on the 2D and massless fermion features of the TSS.

Equation (1) shows the analytical dispersion relationship for the optical plasmon mode in a G/D/G structure or single-layer TI thin film, where ε_1, ε_2, and ε_3 are the permittivities of top, middle, and bottom dielectric media [44,45]. In the case of TI thin films, ε_2 is the permittivity of the bulk. Since TI plasmons are usually excited in the THz frequency range where wavelengths are hundreds of micrometers, real TI thin films ($<1\ \mu$m) will always be in the coupled plasmon regime.

$$\omega_{\text{optical}}^2 = \frac{e^2}{\varepsilon_0}\frac{v_F\sqrt{2\pi n_{2D}}}{h}\frac{q}{\varepsilon_1+\varepsilon_3+qd\varepsilon_2}. \qquad (1)$$

In Eq. (1), $v_F = 5\times10^5$ m/s [1] for TSS in Bi_2Se_3 and $n_{2\text{D}} = 1.2\times10^{13}\ \text{cm}^{-2}$ [35]. Note that $n_{2\text{D}}$ is the sheet carrier concentration of the entire TI thin film and includes the TSS electron contribution from both surfaces. It is clear that when $\varepsilon_{1+}\varepsilon_3 \gg |qd\varepsilon_2|$, the plasmon frequency is proportional to $\sqrt{q}$ and independent of film thickness. In this limit, we recover the dispersion relationship for a single Dirac plasmon layer. However, this condition is not satisfied in most of the experimental measurements of Bi_2Se_3 plasmons [12,16]. For $d = 50$ nm and $q = 0.31\times10^5\ \text{cm}^{-1}$ (corresponding to a 1-μm-wide microribbon), the plasmon frequency is at 4.31 THz [16]. At this frequency, we have $\varepsilon_2 \approx -30$ for bulk Bi_2Se_3; thus, $|qd\varepsilon_2| = 4.6$ and $\varepsilon_{1+}\varepsilon_3 = 12$ for an air superstrate and a sapphire substrate, demonstrating that we are clearly in the coupled plasmon regime where the thickness of TI film matters.

From Eq. (1), we can see that the permittivity of the surrounding environment and of the TI material itself has a significant impact on the plasmon dispersion. A thorough understanding of the optical properties of these materials is therefore needed. In the samples that we will discuss in Sec. IV, we have used c-plane sapphire as the substrate, BIS as a buffer, spacer, and capping layer, air as the superstrate, and Bi_2Se_3 as the TI.

In Eq. (2), we give the frequency-dependent permittivity to model the c-plane sapphire substrate for frequencies below 10 THz where $n_0 = 3.2$, $\lambda = 20.4\times10^{-4}$ cm, and $\gamma = 0.036$ [46].

$$\varepsilon_{Al_2O_3}(\omega) = n_0^2 + \left(n_o^2-1\right)(\lambda\omega)^2 + i\gamma\left(n_o^2-1\right)(\lambda\omega). \qquad (2)$$

The Bi_2Se_3 permittivity can be modeled using Eq. (3), in which the α and β phonons are the contributing Lorentz oscillators:

$$\varepsilon_{Bi_2Se_3}(\omega) = 1 + \frac{S_\alpha^2}{\omega_\alpha^2-\omega^2-i\omega\gamma_\alpha} + \frac{S_\beta^2}{\omega_\beta^2-\omega^2-i\omega\gamma_\beta}, \qquad (3)$$

with $\omega_\alpha = 63.03\ \text{cm}^{-1}$, $S_{\alpha;} = 675.9\ \text{cm}^{-1}$, $\gamma_\alpha = 17.5\ \text{cm}^{-1}$, $\omega_\beta = 126.94\ \text{cm}^{-1}$, $S_\beta = 100\ \text{cm}^{-1}$, $\gamma_\beta = 10\ \text{cm}^{-1}$. Please see Supplemental Material, Sec. I [47], for a detailed discussion of the Bi_2Se_3 permittivity. In Fig. 1(a), we plot the modeled permittivity of Bi_2Se_3 as a function of frequency. We see that the α phonon causes the real part of the permittivity to become large and negative from ~2–10 THz, while the β phonon only causes a small kink near 4 THz. It is important to note that the Bi_2Se_3 permittivity [ε_2 in Eq. (1)] is negative across almost the entire frequency range of interest. In addition to the TI permittivity, we also need to know the BI permittivity to model the layered structure. The optical properties in the visible and mid-IR for different indium compositions of $(Bi_{1\text{-}x}In_x)_2Se_3$ are known [48]. However, the permittivity of BIS in the 2–10-THz range is not known. We obtained the dielectric constant for BIS in this region by fitting the angle-dependent transmission of a 500-nm-thick BIS film under s- and p polarization. The fitting is described in detail in Supplemental Material, Sec. II [47]. The permittivity is described by Eq. (4), where $\varepsilon_{\infty,p} = 10.26$, $\varepsilon_{\infty,s} = 7.40$, $\omega_\alpha = 88.98\ \text{cm}^{-1}$, $S_\alpha = 366.02\ \text{cm}^{-1}$, $\gamma_\alpha = 60.50\ \text{cm}^{-1}$, $\omega_\beta = 142.38\ \text{cm}^{-1}$, $S_\beta = 188.39\ \text{cm}^{-1}$, and $\gamma_\beta = 22.39\ \text{cm}^{-1}$. Here we still describe the two phonon modes observed in BIS as α and β phonons as we assume they are the same vibrational modes that are observed in Bi_2Se_3.

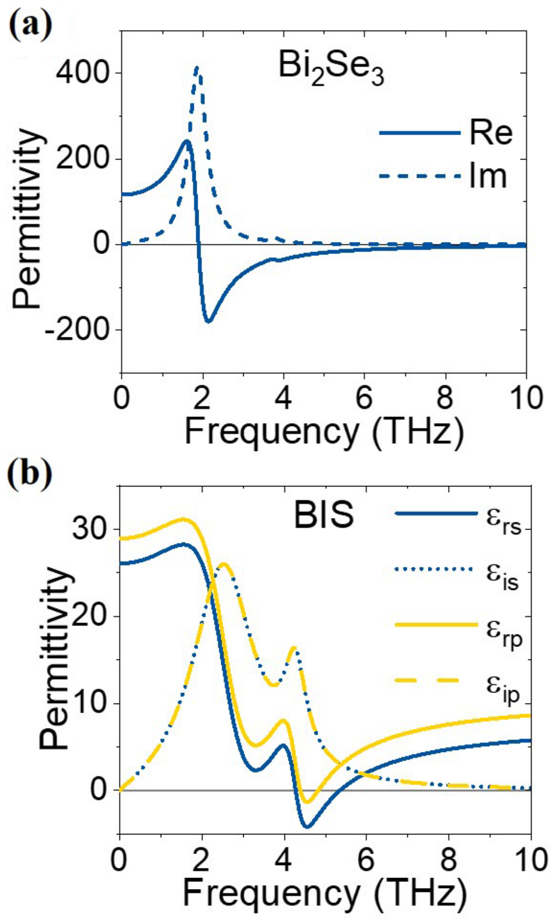

FIG. 1. (a) Real (solid) and imaginary (dashed) parts of the permittivity of Bi_2Se_3 in the THz frequency range. (b) Real (solid) and imaginary (dashed or dotted) parts of the permittivity of BIS for s polarization (blue) and p polarization (yellow) in the THz.

$$\varepsilon_{\text{BIS}}(\omega) = \varepsilon_{\infty,\ p/s} + \frac{S_\alpha^2}{\omega_\alpha^2-\omega^2-i\omega\gamma_\alpha} + \frac{S_\beta^2}{\omega_\beta^2-\omega^2-i\omega\gamma_\beta h}. \qquad (4)$$

Based on the fitting, we plot the permittivity of BIS for both s- and p polarization in Fig. 1(b). The real parts of the permittivity for both polarizations are similar. We note that the real part of the permittivity for *s* polarization is negative in the 4.2–5.3 THz range, while the real part of the permittivity for *p* polarization becomes negative the 4.4–4.8 THz range. This feature will be important for the discussion of the epsilon near-zero (ENZ) mode observed experimentally in Sec. IV.

Now that we know the frequency-dependent permittivity for both the TI and BI layers in our heterostructure, we can model the multilayer material. The exact analytical solution of the plasmon dispersion of multilayer structures relies on a simple form of the Coulomb interaction matrix, which is easy to solve for the case of only two Dirac layers as found in a single TI thin film. However, if the number of interacting Dirac layers increases as N, the Coulomb interaction matrix doubles and $N(N+1)/2$ elements in total are needed to describe the intralayer and interlayer interaction, which makes an analytical solution almost impossible. A good numerical alternative to study optical excitations in these multilayered systems is the TMM, which has successfully been applied to a variety of multilayered optical material stacks. In the next section, we introduce the TMM and apply it to a single TI layer.

III. TRANSFER MATRIX METHOD FOR TOPOLOGICAL INSULATOR PLASMON COUPLING

The TMM relates the electromagnetic (EM) field on one side of a layered structure to the EM field on the other side via sequential multiplication of the transmission matrix D_{N} and the propagation matrix P_{N} for each layer as shown schematically in Figs. 2(a) and 2(b). T matrices have been widely used to study the optical properties in a variety of multilayer films. Transmission, reflection, and absorption from all of the materials and interfaces are combined in the transfer matrix, allowing the transmission and reflection of the entire structure to be calculated as long as the optical properties and thickness of each individual layer are well known. Details of the TMM formalism can be found in Supplemental Material, Sec. III [47]. To model the multilayer structure, we use the permittivities for $\mathrm{Bi_2Se_3}$ and BIS described in Sec. I. We include the TSS as separate infinitesimal two-dimensional conducting layers with finite conductivity σ_{N}, as shown schematically in Fig. 2(a). The optical conductivity in THz range of the TSS has been investigated both theoretically and experimentally [42,49–57] and can be given by

$$\sigma = \frac{e^2}{\hbar^2}\frac{E_F}{4\pi}\frac{i}{\omega + i\tau^{-1}}, \tag{5}$$

$$E_F = \hbar k_F v_F, \tag{6}$$

$$n = \frac{g_s g_v}{4\pi}k_F^2, \tag{7}$$

$$\tau = \mu_m E_F / e {v_F}^2, \tag{8}$$

where E_F is the Fermi energy of the surface states and τ is the relaxation time. For our $\mathrm{Bi_2Se_3}$ grown on a $(\mathrm{Bi_{0.5}In_{0.5}})_2\mathrm{Se_3}$ buffer layer on *c*-plane sapphire, the sheet carrier concentration measured in our films at room temperature $n_{\mathrm{2D}} = 2n_{\mathrm{D}} = 1\times 10^{13}\,\mathrm{cm^{-2}}$ and the mobility is $\mu_{\mathrm{m}} \approx 600\ \mathrm{cm^2\,V^{-1}\,s^{-1}}$ [35]. We assume the majority of the measured carriers can be attributed to the TSS. According to the equations above, we get $E_F \approx 260$ meV above the Dirac point and $\tau \approx 0.06\,\mathrm{ps}$. From the TMM, we can extract the imaginary part of the Fresnel reflection coefficient of the entire structure, Im(r), which indicates loss in the system and can be used to identify plasmon polariton modes [58,59].

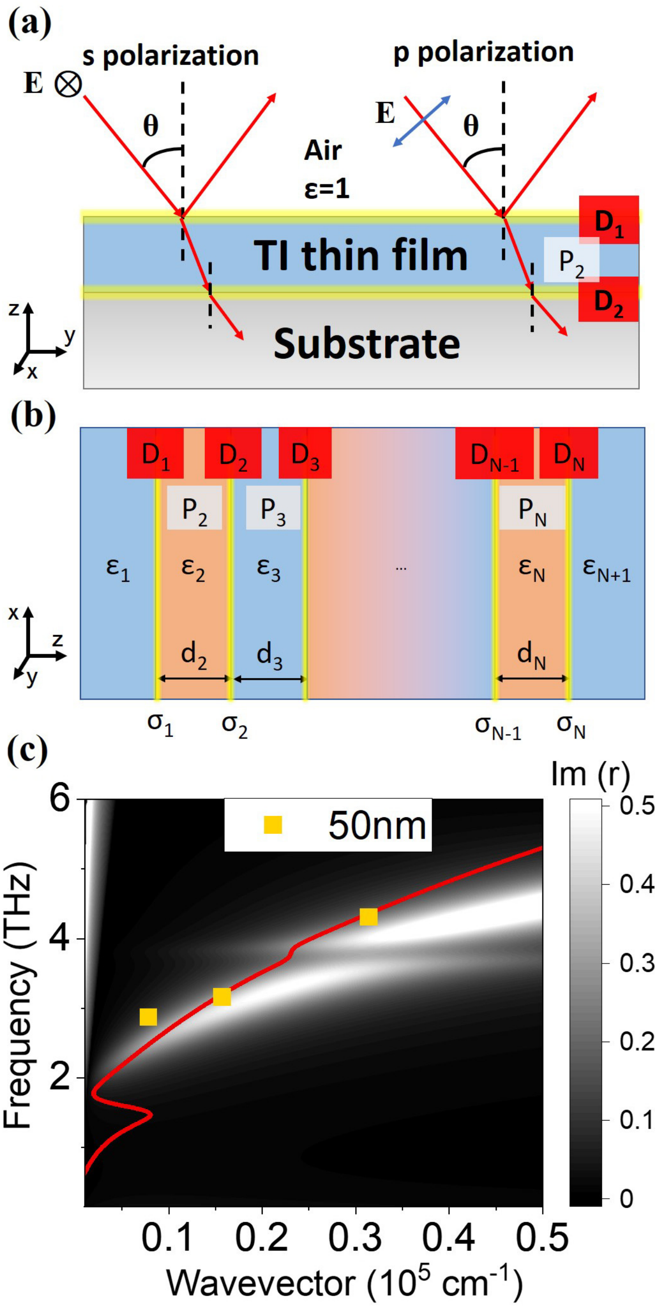

FIG. 2. (a) Schematic of surface states in topological insulator thin films with incident *s*- and *p*-polarization light (not to scale). (b) Schematic of the TMM across multilayer structures with conducting interfaces (yellow). (c) Im(r) calculated using the TMM (color plot) and analytical curve (red solid line) for 50-nm $\mathrm{Bi_2Se_3}$ thin-film plasmon dispersion. Yellow squares are experimental data from Ginley and Law [16].

To demonstrate that the TMM shown schematically in Fig. 2(b) is appropriate to model a multilayer $\mathrm{Bi_2Se_3}$ system, we first test it for a single layer of Bi_2Se_3. In Fig. 2(c), we applied the TMM to a 50-nm layer of Bi_2Se_3 and compared the results to the analytical formula described in Eq. (1) as well as experimental results from Ginley and Law [16]. In this model, as shown in Fig. 2(a), the light is incident from the top through air with $\varepsilon_1 = 1$, and then through the top topological surface, the bulk Bi_2Se_3 with ε_2 described by Eq. (3), the bottom topological surface, and finally the sapphire substrate with ε_3 described by Eq. (2). The bottom sapphire substrate (~0.5 mm in the experiment of Ref. [16]) is modeled as semi-infinite as compared to the thickness of TI films (~50 nm). All of the parameters in the TMM are the same as those used in the analytical expression. The TMM result is shown in the grayscale color plot in Fig. 2(c), which plots $\mathrm{Im}(r)$ as discussed previously. The maxima show the dispersion of the optical mode of the coupled Dirac plasmon system. The analytical results are shown as the red solid line, and the experimental results are shown as the yellow squares. From Fig. 2(c), we observe generally good agreement among the TMM, the analytical model, and the experimental data.

In the color plot, we observe the plasmon strongly coupling to both the α and β phonons, as shown by the kinks in the red analytical curve at the phonon frequencies and by the dark anticrossing features in the TMM color plot at those same frequencies. Similar anticrossing behavior caused by plasmon/phonon interactions has been predicted and observed in bilayer graphene [60–62], graphene h-BN [63–65], graphene-SiO_2 [66], and other heterostructures [67–69]. Added complexity exists in systems like this one in which the plasmon interacts with more than one phonon. For the remainder of this paper, we will refer to modes below the α-phonon frequency (<2 THz) as the lower polariton branch, modes between the α- and β-phonon frequencies (~2–4 THz) as the middle polariton branch, and modes above the β-phonon frequency (>4 THz) as the upper polariton branch. In Fig. 2(c), the relatively broad width of each branch is due to the high damping rate of the three oscillators at room temperature. Due to the stronger interaction between the plasmon and the α phonon, the anticrossing near 2 THz is more obvious and the lower polariton branch is barely visible in the color plot. The interaction between the plasmon and the β phonon is relatively weak with a small gap near the β-phonon frequency. Given the good agreement among the results of the TMM, the analytical model, and the experimental data from Ref. [16], we are confident in the accuracy of the TMM. We can now apply it to more complicated layered heterostructures to investigate plasmon coupling across multiple interfaces. In Supplemental Material, Secs. IV and VIII [47], we show the experimental and modeling results of a single layer of Bi_2Se_3 that is buffered or sandwiched by BIS layer(s). These experiments show that using the BIS capping layer blueshifts the plasmon frequencies as compared with air capping and introduces an ENZ mode near 5.5 THz.

IV. TOPOLOGICAL INSULATOR MULTILAYER STRUCTURES

For a single TI layer, Eq. (1) describes how the optical plasmon mode frequency depends on the film thickness. The thickness dependence arises due to the electrostatic coupling of the TSS plasmons through the TI bulk. However, it has not yet been determined if the TSS in one TI layer can couple to the TSS in a different TI layer across a BI. Using BIS which is structurally compatible with Bi_2Se_3, we are able to create a sample with multiple separated TSS. The structures we investigate comprise a BIS buffer layer, a Bi_2Se_3 layer, a BIS spacer layer, a second Bi_2Se_3 layer, and a BIS capping layer. The whole five-layer structure is shown schematically in Fig. 3(a). Since the plasmon modes in the TI layered structure have wave vectors much larger than light in free space, the as-grown films are fabricated into periodic microribbon arrays with designated widths using standard lithographic and ion-milling techniques to excite localized plasmon polaritons. The wave vector of the plasmon polariton excited in the microribbon is given by $k = \pi/a$, where a is the width of the ribbons. The widths of the ribbons are confirmed with atomic force microscopy (AFM) measurements. The thickness of each layer is determined using growth-rate calibration results for Bi_2Se_3 and BIS separately. We measure the extinction spectrum of each sample at normal incidence using Fourier transform infrared (FTIR) spectroscopy. The extinction is calculated using $1 - T/T_0$, where T and T_0 are the transmission of the sample and the bare substrate, respectively. FTIR spectra were taken for both transverse electric polarized light (TE mode, **E** parallel to ribbon) and transverse magnetic polarized light (TM mode, **E** perpendicular to ribbon). The localized surface plasmon mode can only be excited by TM-polarized light; in the TE-polarized data, only the α-and β-phonon peaks are visible.

For this coupled two-layer system, we investigate the effect of changing three structural parameters: ribbon width which changes the wave vector and allows mapping of the polariton dispersion (series A, B); the center BIS spacer-layer thickness to understand how the TSS couple across a trivial insulator (series C); and the Bi_2Se_3 layer thicknesses to understand how the TSS couple across multiple topological insulators (series D). When one parameter is changed, the other two are held constant. In series A, the buffer layer, spacer layer, and capping layer of BIS are all held at 50 nm while the two Bi_2Se_3 layers are at 60 nm. In series B, we keep the buffer and capping BIS layer at 50 nm but increase the spacer layer to 150 nm. The Bi_2Se_3 layers are 50 nm in series B. In series A and B, the ribbon widths vary from 0.5–10 μm. In series C, we vary the spacer-layer thickness from 10 to 300 nm and keep the Bi_2Se_3 layer thickness at 50 nm and ribbon widths at 6 μm. In series D, we vary the Bi_2Se_3 layer thickness from 20 to 200 nm, while the BIS layers are held constant at 50 nm and the ribbon widths at 6 μm. After nanofabrication of the as-grown samples into periodic microribbon arrays, we measured the TM extinction spectra. At least two peaks are shown for all samples in the range of 1.5–8 THz. By changing the three structural parameters in this system, we observe frequency shifts in the polariton modes. This allows us to map out the dispersion of these coupled modes as a function of wave vector, spacer thickness, and TI layer thickness.

A cross-sectional transmission electronic microscopy (TEM) image of series A is shown in Fig. 3(b). Clear interfaces between the Bi_2Se_3 and BIS layers are seen with good contrast. The thicknesses of the bottom and top Bi_2Se_3 layers are measured to be 57.4 and 59.7 nm, respectively, close to

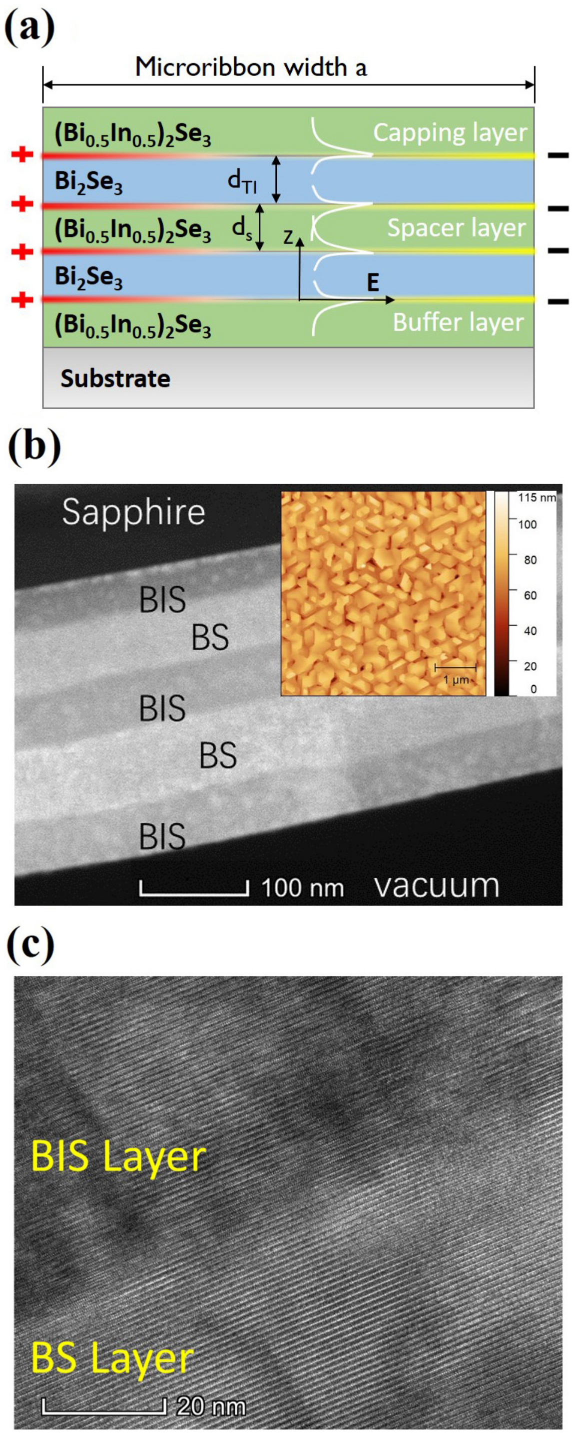

FIG. 3. (a) Schematic of the two-layer Bi_2Se_3 plasmon coupling structure. The white lines indicate the electric field coupling across the layers. (b) TEM image of the structure in series A. Distinct layers are clearly observed. BS is abbreviation for Bi_2Se_3. Inset: AFM image of series A. Scan size: 5 μm × 5 μm. (c) High resolution TEM image of the quintuple layers in series A.

the desired thickness for series A. The wavelike feature in the image is an artifact caused by the focused ion-beam etching. The inset shows an AFM picture of the unpatterned sample with characteristic triangular-shaped domains of the top BIS capping layer. TEM pictures with higher magnification in Fig. 3(c) show the high crystallinity of each atomic layer.

We will first discuss series A and series B. Films from both series were patterned into microribbon arrays with ribbon widths ranging from $a = 0.5$ to 10 μm, after which their extinction spectra were measured. In Figs. 4(a) and 4(d), the empty symbols are the TM-polarized extinction spectra that were multiplied (abbreviated as M) and then offset (abbreviated as O) for better visualization. At least two peaks are shown for all samples, indicating a double Fano resonance. We use an analytical Fano fitting procedure to extract the peak positions and widths, assuming the two polariton modes are Lorentz oscillators. Details of the Fano fitting can be found in Supplemental Material, Secs. IV and V [47]. In the fitting, the α-phonon frequency, ω_α, is fixed at 2.00 or 2.01 THz based on the measured phonon peak in the corresponding TE spectrum (included in Supplemental Material, Sec. VII [47]. The fitting curve for each spectrum is shown as a solid black curve.

In Fig. 4(a), we can clearly distinguish two peaks for the series A samples with $a = 4\,\mu$m and $a = 2.3$ μm, but for the sample with $a = 1.5$ μm, we only observe one broad peak. The same trend is also observed for series B shown in Fig. 4(d). Despite the observation of one peak, we find that this peak cannot be fitted well with a single Lorentz oscillator. We therefore still use two Lorentz oscillators to fit this feature in both series A and series B. When the nanoribbons narrow further, the two peaks reemerge and split. Samples $a =$ 1.5 μm and $a = 1$ μm show a small bump at around 2 THz, which does not appear in other samples. This peak is near the bare α-phonon frequency and is part of the lower polariton branch. In these samples, because the plasmon polariton is at a relatively high frequency, the lower polariton branch is near the bare α-phonon frequency and the lower polariton mode has primarily α-phonon character. This peak does not appear in the two narrowest ribbons in series A ($a = 0.75$ μm and $a = 0.5$ μm) or in any of the narrow series B samples which can be attributed to a small peak strength and a low signal to noise ratio in this spectral range in these samples.

The mode frequencies as a function of wave vector for series A are plotted in Fig. 4(b) on top of a color plot of Im(r) calculated using the TMM. A similar plot is shown for series B in Fig. 4(e). The middle polariton branch (blue circles) and upper polariton branch (yellow squares) both shift to higher frequencies as the wave vector increases. This is the same trend that we observe in the single-layer Bi_2Se_3. The shift to higher frequencies with increasing wave vector can be explained phenomenologically by realizing that we are exciting a standing-wave mode. As the ribbons become narrower, the wavelength of the standing-wave polariton mode will decrease and its frequency will increase. For wave vectors above 0.2×10^5 cm^{-1}, the middle polariton branch becomes too weak to observe experimentally. We instead begin to excite the BIS ENZ mode (green triangles) near 5.5 THz described in Sec. III. The ENZ mode is a polaritonic mode that is often observed in plasmonic materials or polar dielectric thin films when the permittivity of the material is close to zero. For the latter, the real part of permittivity often crosses zero close to the longitudinal optical phonon frequency, which is the case for BIS as described in Sec. II and shown in Fig. 1(b).

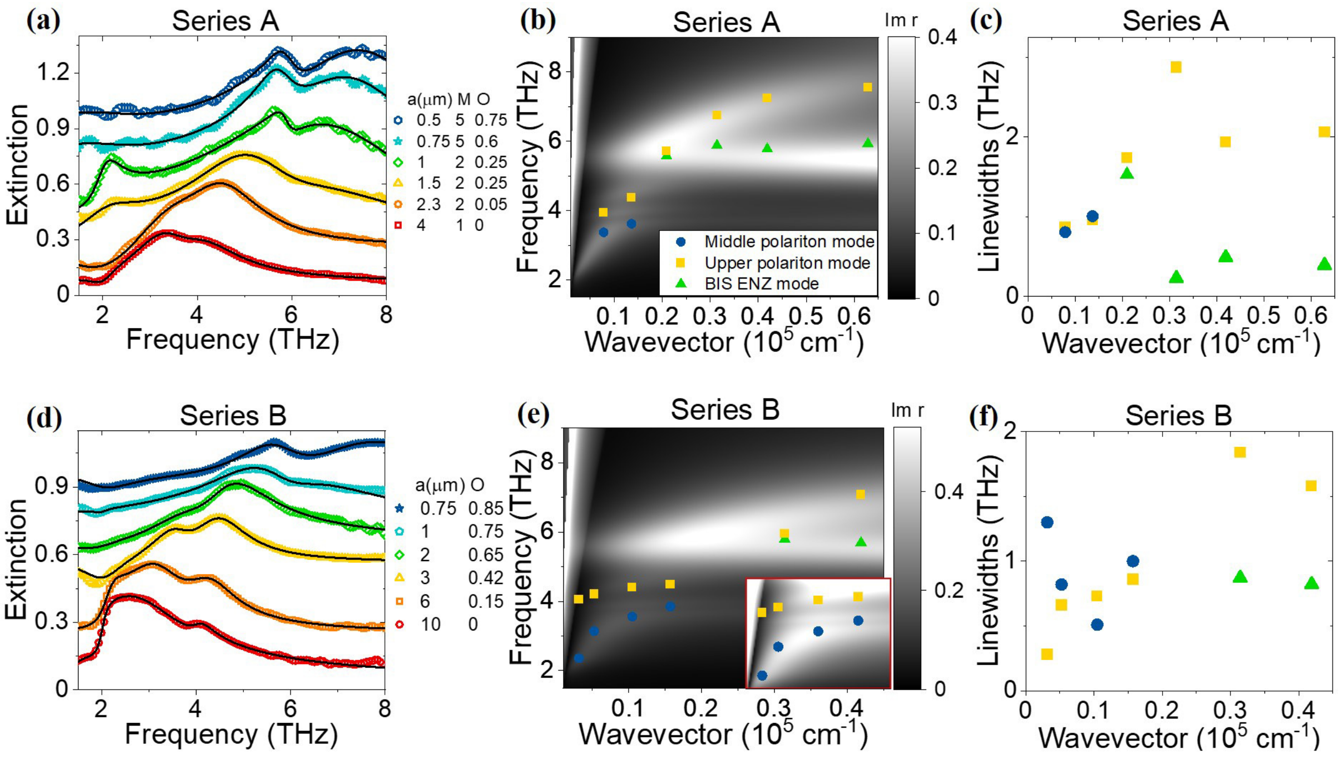

FIG. 4. (a), (d) Extinction spectra for series A and B, respectively. Black solid curves are the three oscillator Fano resonance fitting of the experimental data (open symbols). Data multiplication (M) and offset (O) are used for better visualization. (b), (e) Color plot: TMM of series A and B. The experimental upper polariton mode (yellow squares), middle polariton mode (blue circles), and BIS ENZ mode (green triangles) extracted from Fano resonance fitting are shown for comparison. Inset of (e) is a zoom-in at low wave vectors with adjusted color scale. Anticrossing caused by plasmon-phonon interaction is clearly seen. (c), (f) Linewidths of the polariton modes in series A and B extracted from the Fano resonance fitting. Symbols correspond to those in panels (b), (e).

The linewidths of all modes are extracted from the data fitting and plotted in Figs. 4(c) and 4(f). We find that at wave vectors below 0.2×10^5 cm^{-1}, the linewidths for the two modes are similar. This is consistent with the attribution of these modes to the middle and upper polariton branches. These two polariton branches are mainly caused by plasmon–"β-phonon" interaction, which is illustrated well by the anticrossing shown in the inset of Fig. 4e). We note that the β-phonon mode in this layered material is actually a combination of the Bi_2Se_3 β phonon and the BIS β phonon which have slightly different frequencies, which can be seen as the gaps in the inset of Fig. 4(e). However, for wave vectors above 0.2×10^5 cm^{-1}, the lower-frequency mode shows a much narrower linewidth than the higher-frequency mode. The higher-frequency mode is attributed to the upper polariton branch as it continues the trend for plasmon dispersion; a relatively large linewidth is expected for this mode and is consistent with other TI plasmon polariton observations [12,16]. The narrower linewidth of the lower-frequency mode is consistent with the attribution of this peak to the BIS ENZ mode.

Extra optical plasmon modes are direct evidence of plasmon coupling. However, in series A and B, we only observe one plasmon branch instead of the four expected branches caused by coupling among the four TSS. The other three branches are damped by phonon coupling and scattering. We illustrate this point by comparing the structure to a multilayer graphene plasmonic system in Supplemental Material, Sec. X [47]. Although we only see the brightest plasmon mode in our samples, we can still see the effect of multiple TSS coupling in the change in the dispersion curve. In Supplemental Material, Sec. IX [47], we compare the analytical curves for single-layer Bi_2Se_3 to the experimental plasmon dispersion curves in series A and B. We observe an obvious blueshift in the experimental data due to coupling among the four TSS.

To fully characterize coupling in a multilayer system, we must also understand the effect of changing the multilayer structural parameters. In our case, the relevant parameters are the thickness of the TI layers (d_{TI}) and the thickness of the BIS spacer layer (d_s). Series C and D are thus grown to understand the plasmon mode dependence on the BIS spacer layer and TI layer thicknesses, respectively, which should change the strength of the coupling among the TSS.

In series C, we change the BIS spacer thickness d_s while keeping a constant $a = 6$ μm ribbon width and a constant $d_{\mathrm{TI}} = 50$ nm Bi_2Se_3 layer thickness. The data for this series are shown in Fig. 5. In this series, the α-phonon peak position is not kept constant in the fitting but allowed to vary within a range of 1.99 to 2.15 THz. We observe a blueshift of the α-phonon frequency when $d_s > 150$ nm. This is consistent with the TE-polarized data shown in Supplemental Material, Sec. VII [47]. This blueshift is caused by the increasing amount of indium in the total structure. Since indium has a lower atomic weight than bismuth, it is not surprising that the

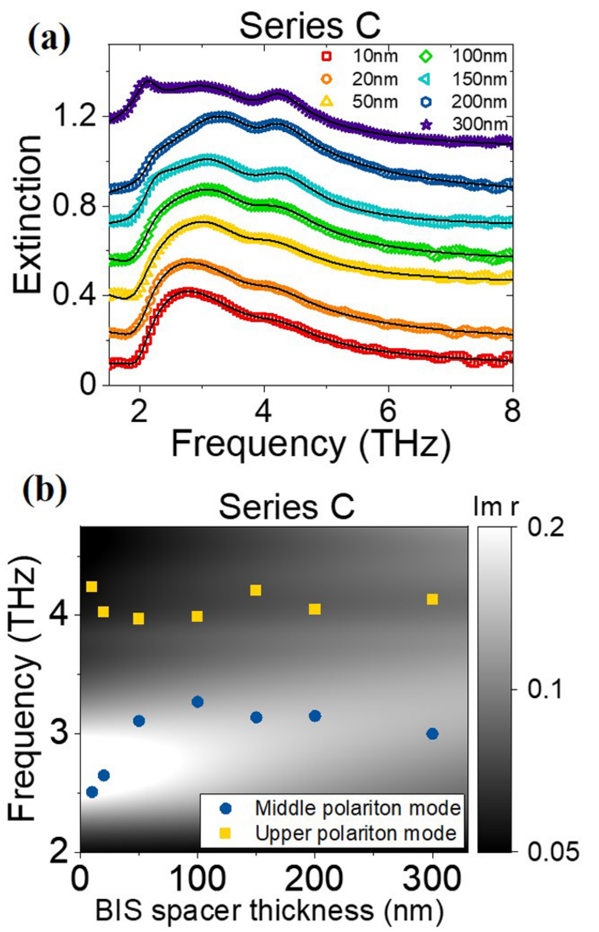

FIG. 5. (a) Extinction spectra of series C. Black solid curves show the three oscillator Fano resonance fitting of the experimental data (open symbols). The curves are offset increasingly by multiples of 0.15 for ease of visualization. (b) Color plot shows TMM modeling for series C. Blue circles (yellow squares) indicate the middle (upper) polariton branch modes.

phonon frequencies blueshift slightly. We do not observe two separate phonon frequencies from the $\mathrm{Bi_2Se_3}$ and BIS layers since the frequency shift is smaller than the linewidth of the resonance. In addition, the ENZ mode is not excited in series C and D due to the small wave vector.

For samples with thin spacers ($d_s < 100\,\mathrm{nm}$), we only observe two distinct modes in Fig. 5(a), but for samples with $d_s > 100\,\mathrm{nm}$, we observe three clear peaks. We attribute the narrow peak near 2 THz to uncoupled α-phonon absorption in the thick BIS spacer layer. Although we expect the plasmon to strongly couple to both the α- and β phonons, if the BIS spacer is so thick that the evanescent plasmon electric field does not extend throughout the layer, we would expect to observe a reemergence of the BIS phonon peaks. As the spacer-layer thickness increases, the middle polariton branch [blue circles in Fig. 5(b)] blueshifts for spacer thicknesses below 100 nm and then slightly redshifts for spacer thicknesses above 100 nm. The upper polariton branch [yellow squares in Fig. 5(b)] is almost constant over the entire range of thicknesses, with a small blueshift with decreasing thickness for the thinnest spacers. However, the TMM data, as shown in Fig. 5(b), predict constant-frequency middle and upper polariton branches as a function of spacer thickness.

The disagreement between experiment and modeling at small spacer thicknesses could be caused by a variety of effects, but the most likely explanation is penetration of the TSS wave function into the BIS barrier. At an interface between $\mathrm{Bi_2Se_3}$ and $\mathrm{BiInSe_3}$, the TSS wave function has been measured to extend approximately 50 nm into the $\mathrm{Bi_{0.5}In_{0.5}Se_3}$ layer [70]. When the spacer is thicker than 50 nm, the TSS are quantum mechanically decoupled and the plasmon coupling will only arise through the electrostatic interaction which is captured by the TMM. However, if the spacer is thinner than 50 nm, the overlap of the TSS wave functions will add additional complexity to the optical response of the heterostructure not captured by the TMM. Since we see the deviation between experiment and the TMM arise when the spacer thickness is less than 50 nm, the attribution of this deviation to the TSS wave function overlap is reasonable.

Since the bulk TI and BI materials are topologically distinct and have different optical dielectric constants, we expect the Dirac plasmon dispersion dependence on the TI and BI thickness to be different. Therefore, in series D, we changed the $\mathrm{Bi_2Se_3}$ thickness d_{TI} but kept the BIS spacer-layer thickness constant at $d_s = 50\,\mathrm{nm}$ and the microribbon width constant at $a = 6\,\mu\mathrm{m}$. As shown in Fig. 6, the middle polariton mode blueshifts significantly as the $\mathrm{Bi_2Se_3}$ layer thickness increases. This is not unexpected. In single $\mathrm{Bi_2Se_3}$ layers, the plasmon polariton frequency blueshifts with increasing thickness, as observed in Ref. [16] and as shown in Eq. (1) due to the negative real part of the $\mathrm{Bi_2Se_3}$ permittivity. For the upper polariton mode, the TMM predicts its nearly constant frequency, while the intensity increases with increasing $\mathrm{Bi_2Se_3}$ thickness. This is because at small wave vector and small $\mathrm{Bi_2Se_3}$ thickness, the plasmon frequency is far from the β phonon, so the upper polariton mode has a strong β-phonon character resulting in an intensity that is too weak to be seen easily on the color plot. In contrast, as the $\mathrm{Bi_2Se_3}$ thickness increases above 50 nm, the plasmon frequency approaches the β phonon and strongly couples, generating a hybridized plasmon-phonon polariton. In this case, the upper polariton branch has a strong plasmon character, so we easily see the mode on the color plot. In general, the experimental data match the modeling well. However, for $\mathrm{Bi_2Se_3}$ layer thickness less than 50 nm, we see the upper polariton mode deviate from the prediction. This deviation can be attributed to a combined effect of the β-phonon shift and strong coupling among the TSS: with decreasing $\mathrm{Bi_2Se_3}$ thickness, the β phonon blueshifts and at the same time the TSS coupling gets stronger.

We would like to point out several assumptions that we made in the TMM as they may cause some of the minor discrepancies between the experimental data and the TMM. First, we assumed that the chemical potential of the TSS at all $\mathrm{Bi_2Se_3}$-BIS interfaces are equal. This is reasonable as the two layers of $\mathrm{Bi_2Se_3}$ are identical and encapsulated by BIS. Second, we assumed that the carrier concentration determined by transport measurements arises mainly from the Dirac electrons, so we only need to consider Dirac plasmons in our TMM. Stauber *et al.* [71] proposed to add in a massive 2DEG plasmon response to get a closer fit to the experimental data of Ref. [12] which showed discrepancies at large wave vectors.

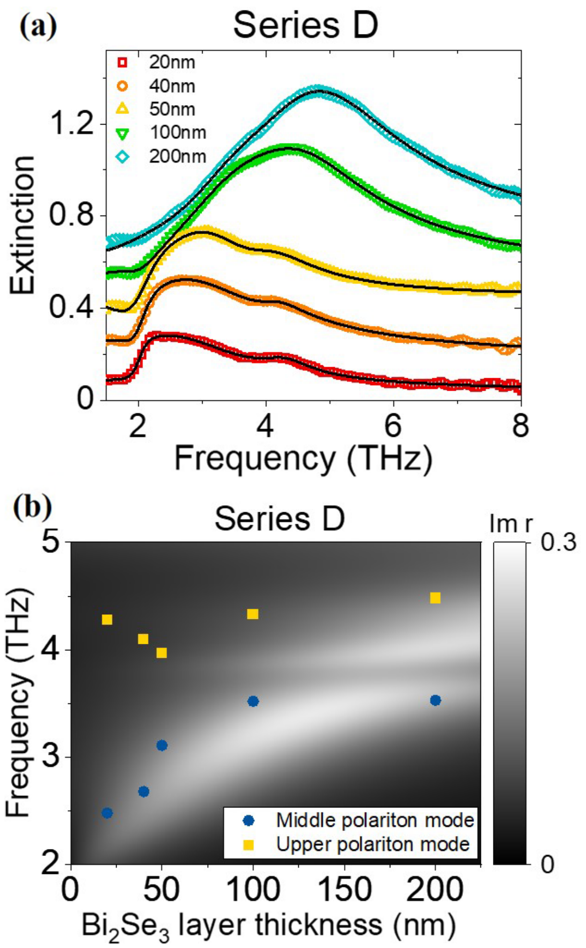

FIG. 6. (a) Extinction spectra of series D. Black solid curves show the three oscillator Fano resonance fitting of the experimental data (open symbols). The curves are offset increasingly by multiples of 0.15 for ease of visualization. (b) Color plot shows TMM modeling for series D. Blue circles (yellow squares) indicate the middle (upper) polariton branch modes.

However, in this case, the Bi_2Se_3 layers are encapsulated with BIS, hopefully reducing or eliminating the band-bending effect. In addition, other transport and optical measurements on Bi_2Se_3 have shown that the TSS contributes 70–90% of the electron response [72,73], so it is reasonable to assume that the major contribution to the plasmonic response observed in our samples is from the Dirac electrons. Third, we model the TSS as infinitesimal conducting layer, which is acceptable for most samples given that the TSS penetration depth in Bi_2Se_3 is usually 2–3 nm [42,43]. However, this approximation may lose validity in cases like those described in series C where the TSS penetration depth increases significantly. Fourth, we neglected the dipole-dipole interaction between patterned ribbons, which could cause a redshift, especially with small periodicities [74–76]. Finally, the interlayer spin-orbit coupling could modify the plasmon dispersion [77]; this effect is not included in the TMM. Despite these caveats, the general good agreement between the TMM predictions which assume electrostatic interactions among all four TSS and the experimental data indicates that we are observing coupling among all four TSS in this multilayer structure.

V. CONCLUSION

Coupling among plasmon polaritons and phonons in a superlattice comprising the topological insulator Bi_2Se_3 and the trivial insulator $(Bi_{0.5}In_{0.5})_2Se_3$ has been observed. The dispersion of these hybrid modes was shown to depend on the wave vector, TI thickness, and band insulator thickness in the THz range. We showed that the transfer matrix method can be used to model the optical properties of such structures with general success, especially at low wave vectors. In structures with thin TI and BI layers, we observe strong coupling among the plasmon modes in the four topological surface states. In the future, adjusting the ratio of TI to BI will enable tuning of the optical properties of the structure. Adding more layers could result in a wafer-scale Dirac metamaterial in the THz. This work has laid the foundation for future research into the properties of TI superlattices.

ACKNOWLEDGMENT

This project is supported by the U.S. Department of Energy, Office of Science, Office of Basic Energy Sciences, under Award No. DE-SC0017801.

APPENDIX

1. Heterostructure growth

All films were epitaxially grown on (0001)-oriented single-side polished 1 cm × 1 cm sapphire in a dedicated Veeco GenXplor molecular-beam epitaxy chamber. Bismuth and indium fluxes are generated in dual-filament Knudson effusion cells and monitored via beam-flux monitoring with a tungsten filament, while the selenium flux is generated with a cracking cell to ensure efficient incorporation into the film [34]. The quality of the as-grown crystal is monitored by *in situ* real-time reflection high energy electron diffraction measurement. The sapphire substrates were baked at 200 °C in the load lock for 12 h before transferring into the growth chamber. The substrates were then heated to 650 °C as measured by a thermocouple for outgassing and cooled down to 300 °C for the growth of the first five quintuple layers (QL) Bi_2Se_3, followed by subsequent growth of five QL In_2Se_3. The flux is controlled for a constant growth rate of 0.8 nm/min. This bilayer was then annealed at 425 °C for 40 min to form a single seed layer of $(Bi_{0.5}In_{0.5})_2Se_3$ with high crystallinity [35]. The remaining 40 nm $(Bi_{0.5}In_{0.5})_2Se_3$ was codeposited at the optimal growth temperature of 425 °C. After this layer, the substrate was cooled back to 300 °C for Bi_2Se_3 film growth with desired thickness. The spacer layer of BIS was then directly codeposited at 300 °C to maintain the crystallinity of the Bi_2Se_3. If we heat the sample for the BIS growth, selenium atoms will outgas, causing roughening of the top surface of Bi_2Se_3, which will introduce extra unwanted carriers. On the other hand, $(Bi_{0.5}In_{0.5})_2Se_3$ grown at 300 °C has smaller domains than BIS grown at a higher temperature, but there is very little effect on the electronic properties of the Bi_2Se_3 layer grown on top of it. The top layer of Bi_2Se_3 was kept at the same thickness as the bottom Bi_2Se_3 layer to keep the structure symmetric. The final capping layer of 50 nm $(Bi_{0.5}In_{0.5})_2Se_3$ was applied to maintain a symmetric structure as well as to protect the TSS from atmosphere or any other surface damage during the nanofabrication process. After growth, the sample was sealed in vacuum pack while awaiting further nanofabrication and characterization.

2. Growth of $(Bi_{0.5}In_{0.5})_2Se_3$ film for optical measurement

A 500 nm single-crystal film of $(Bi_{0.5}In_{0.5})_2Se_3$ is grown on sapphire substrate via codeposition in the MBE. A 5 nm layer of Bi_2Se_3 and 5 nm In_2Se_3 were sequentially deposited and annealed for 40 min to form a seed layer; the rest of the film was deposited at 425 °C. The thickness of the film was confirmed with calibrated growth rate for $(Bi_{0.5}In_{0.5})_2Se_3$ as well as profilometry measurements.

3. Film patterning

All samples were patterned into microribbon arrays using standard UV photolithography or e-beam lithography. After resist development, all patterned films were dry etched with argon ion milling through to the sapphire substrate. The remaining resist was removed by soaking the samples in N-Methyl-2-Pyrrolidone.

4. Extinction measurements

A Bruker Vertex 70v Fourier transform infrared spectrometer was used for normal transmission measurements at room temperature. Spectra were taken under vacuum. A terahertz polarizer was used to separately measure the TE and TM spectra of the patterned structures. Both the background and sample transmission were taken at the same polarizer angle, room temperature (23 °C), and room humidity around 42%. Data are taken at 1.6 kHz scan velocity and 4 cm^{-1} resolution.

5. Microscopy measurements

The TEM sample of the cross-sectional area of the multilayer film was prepared via a focused ion-beam lift-out approach (Zeiss Auriga 60 CrossBeam SEM) and an amorphous carbon layer was intentionally deposited on the top of the sample by gas injection system inside the SEM as a protective film. The layer thickness and interfacial structure were characterized by using TEM. TEM images were collected at an accelerating voltage of 200 kV by a Talos^{TM} F200 C TEM.

[1] H. Zhang, C.-X. Liu, X.-L. Qi, X. Dai, Z. Fang, and S.-C. Zhang, Nat. Phys. **5**, 438 (2009).

[2] X. Zhang, J. Wang, and S. C. Zhang, Phys. Rev. B **82**, 245107 (2010).

[3] W. Tang, A. Politano, C. Guo, W. Guo, C. Liu, L. Wang, X. Chen, and W. Lu, Adv. Funct. Mater. **28**, 1801786 (2018).

[4] L. Viti, D. Coquillat, A. Politano, K. A. Kokh, Z. S. Aliev, M. B. Babanly, O. E. Tereshchenko, W. Knap, E. V. Chulkov, and M. S. Vitiello, Nano Lett. **16**, 80 (2016).

[5] C. W. Luo, H. J. Chen, C. M. Tu, C. C. Lee, S. A. Ku, W. Y. Tzeng, T. T. Yeh, M. C. Chiang, H. J. Wang, W. C. Chu, J. Y. Lin, K. H. Wu, J. Y. Juang, T. Kobayashi, C. M. Cheng, C. H. Chen, K. D. Tsuei, H. Berger, R. Sankar, F. C. Chou, and H. D. Yang, Adv. Opt. Mater. **1**, 804 (2013).

[6] H. P. Paudel and M. N. Leuenberger, Phys. Rev. B **88**, 085316 (2013).

[7] I. Vobornik, U. Manju, J. Fujii, F. Borgatti, P. Torelli, D. Krizmancic, Y. S. Hor, R. J. Cava, and G. Panaccione, Nano Lett. **11**, 4079 (2011).

[8] D. Pesin and A. H. MacDonald, Nat. Mater. **11**, 409 (2012).

[9] A. Politano, L. Viti, and M. S. Vitiello, APL Mater. **5**, 035504 (2017).

[10] A. N. Grigorenko, M. Polini, and K. S. Novoselov, Nat. Photonics **6**, 749 (2012).

[11] T. Stauber, G. Gómez-Santos, and L. Brey, Phys. Rev. B **88**, 205427 (2013).

[12] P. Di Pietro, M. Ortolani, O. Limaj, A. Di Gaspare, V. Giliberti, F. Giorgianni, M. Brahlek, N. Bansal, N. Koirala, S. Oh, P. Calvani, and S. Lupi, Nat. Nanotechnol. **8**, 556 (2013).

[13] A. Politano, C. Lamuta, and G. Chiarello, Appl. Phys. Lett. **110**, 211601 (2017).

[14] A. Politano, V. M. Silkin, I. A. Nechaev, M. S. Vitiello, L. Viti, Z. S. Aliev, M. B. Babanly, G. Chiarello, P. M. Echenique, and E. V. Chulkov, Phys. Rev. Lett. **115**, 216802 (2015).

[15] A. Kogar, S. Vig, A. Thaler, M. H. Wong, Y. Xiao, D. Reig-i-Plessis, G. Y. Cho, T. Valla, Z. Pan, J. Schneeloch, R. Zhong, G. D. Gu, T. L. Hughes, G. J. MacDougall, T.-C. Chiang, and P. Abbamonte, Phys. Rev. Lett. **115**, 257402 (2015).

[16] T. P. Ginley and S. Law, Adv. Opt. Mater. **6**, 1800113 (2018).

[17] M. Zhao, M. Bosman, M. Danesh, M. Zeng, P. Song, Y. Darma, A. Rusydi, H. Lin, C. W. Qiu, and K. P. Loh, Nano Lett. **15**, 8331 (2015).

[18] A. M. Dubrovkin, G. Adamo, J. Yin, L. Wang, C. Soci, Q. J. Wang, and N. I. Zheludev, Adv. Opt. Mater. **5**, 1600768 (2017).

[19] M. Autore, F. D. Apuzzo, A. Di Gaspare, V. Giliberti, O. Limaj, P. Roy, M. Brahlek, N. Koirala, S. Oh, F. Javier, G. De Abajo, and S. Lupi, Adv. Opt. Mater. **3**, 1257 (2015).

[20] S. V. Dordevic, M. S. Wolf, N. Stojilovic, H. Lei, and C. Petrovic, J. Phys.: Condens. Matter **25**, 075501 (2013).

[21] W. Richter, H. Kohler, and C. R. Becker, Phys. Status Solidi **84**, 619 (1977).

[22] P. Sohr, D. Wei, S. Tomasulo, M. K. Yakes, and S. Law, ACS Photonics **5**, 4003 (2018).

[23] D. Wei, C. Harris, and S. Law, Opt. Mater. Express **7**, 2672 (2017).

[24] J.-J. Zhu, S. M. Badalyan, and F. M. Peeters, Phys. Rev. B **87**, 085401 (2013).

[25] S. M. Badalyan and F. M. Peeters, Phys. Rev. B **85**, 195444 (2012).

[26] P. Wachsmuth, R. Hambach, G. Benner, and U. Kaiser, Phys. Rev. B **90**, 235434 (2014).

[27] H. Yan, X. Li, B. Chandra, G. Tulevski, Y. Wu, M. Freitag, W. Zhu, P. Avouris, and F. Xia, Nat. Nanotechnol. **7**, 330 (2012).

[28] J. Xu, W. Pan, S. Zhang, N. Liu, Y. Lu, and Z. Liang, Opt. Eng. **59**, 017104 (2020).

[29] Y. Chang, C. Liu, C. Liu, S. Zhang, and S. R. Marder, Nat. Commun. **7**, 10568 (2016).

[30] H. D. Li, Z. Y. Wang, X. Guo, T. L. Wong, N. Wang, and M. H. Xie, Appl. Phys. Lett. **98**, 043104 (2011).

[31] Z. Chen, L. Zhao, K. Park, T. A. Garcia, M. C. Tamargo, and L. Krusin-Elbaum, Nano Lett. **15**, 6365 (2015).

[32] Z. Y. Wang, X. Guo, H. D. Li, T. L. Wong, N. Wang, and M. H. Xie, Appl. Phys. Lett. **99**, 023112 (2011).
[33] Y. Zhao, H. Liu, X. Guo, Y. Jiang, Y. Sun, H. Wang, Y. Wang, H. D. Li, M. H. Xie, X. C. Xie, and J. Wang, Nano Lett. **14**, 5244 (2014).
[34] T. P. Ginley and S. Law, J. Vac. Sci. Technol. B **34**, 02L105 (2016).
[35] Y. Wang, T. P. Ginley, and S. Law, J. Vac. Sci. Technol. B **36**, 02D101 (2018).
[36] H. D. Lee, C. Xu, S. M. Shubeita, M. Brahlek, N. Koirala, S. Oh, and T. Gustafsson, Thin Solid Films **556**, 322 (2014).
[37] M. Brahlek, N. Bansal, N. Koirala, S. Y. Xu, M. Neupane, C. Liu, M. Z. Hasan, and S. Oh, Phys. Rev. Lett. **109**, 186403 (2012).
[38] E. H. Hwang and S. Das Sarma, Phys. Rev. B **80**, 205405 (2009).
[39] R. E. V Profumo, R. Asgari, M. Polini, and A. H. MacDonald, Phys. Rev. B **85**, 085443 (2012).
[40] R. E. V Profumo, M. Polini, R. Asgari, R. Fazio, and A. H. MacDonald, Phys. Rev. B **82**, 085443 (2010).
[41] B. Scharf and A. Matos-Abiague, Phys. Rev. B **86**, 115425 (2012).
[42] L. L. Li, W. Xu, and F. M. Peeters, J. Appl. Phys. **117**, 175305 (2015).
[43] Y. Zhang, K. He, C. Z. Chang, C. L. Song, L. L. Wang, X. Chen, J. F. Jia, Z. Fang, X. Dai, W. Y. Shan, S. Q. Shen, Q. Niu, X. L. Qi, S. C. Zhang, X. C. Ma, and Q. K. Xue, Nat. Phys. **6**, 584 (2010).
[44] T. Stauber, J. Phys.: Condens. Matter **26**, 123201 (2014).
[45] Y. Deshko, L. Krusin-Elbaum, V. Menon, A. Khanikaev, and J. Trevino, Opt. Express **24**, 7398 (2016).
[46] S. Roberts and D. D. Coon, J. Opt. Soc. Am. **52**, 1023 (1962).
[47] See Supplemental Material at http://link.aps.org/supplemental/10.1103/PhysRevMaterials.4.115202 for details on optical modeling and additional experimental spectra. References [78–89] are cited in the Supplemental Material.
[48] Y. Wang and S. Law, Opt. Mater. Express **8**, 2570 (2018).
[49] F. Parhizgar, A. G. Moghaddam, and R. Asgari, Phys. Rev. B **92**, 045429 (2015).
[50] X. Xiao and W. Wen, Phys. Rev. B **88**, 045442 (2013).
[51] X. Wang, J. Lian, Y. Huang, Z. Sun, J. Liu, F. Zhang, S. Gao, X. Yu, P. Li, and M. Zhao, Jpn. J. Appl. Phys. **52**, 103001 (2013).
[52] W. K. Tse and A. H. MacDonald, Phys. Rev. Lett. **105**, 057401 (2010).
[53] L. S. Huang, H. M. Dong, Y. F. Duan, J. L. Liu, and C. X. Zhao, Appl. Opt. **57**, 9275 (2018).
[54] M. Lasia and L. Brey, Phys. Rev. B **90**, 075417 (2014).
[55] Z. Li and J. P. Carbotte, Phys. Rev. B **88**, 045414 (2013).
[56] A. D. LaForge, A. Frenzel, B. C. Pursley, T. Lin, X. Liu, J. Shi, and D. N. Basov, Phys. Rev. B **81**, 125120 (2010).
[57] J. Qi, H. Liu, and X. C. Xie, Phys. Rev. B **89**, 155420 (2014).
[58] M. S. Vasconcelos and M. G. Cottam, J. Phys. D: Appl. Phys. **52**, 285104 (2019).
[59] J. Madrigal-Melchor, J. S. Pérez-Huerta, J. R. Suárez-López, I. Rodríguez-Vargas, and D. Ariza-Flores, Superlattices Microstruct. **125**, 247 (2019).
[60] F. J. Bezares, A. De Sanctis, J. R. M. Saavedra, A. Woessner, P. Alonso-González, I. Amenabar, J. Chen, T. H. Bointon, S. Dai, M. M. Fogler, D. N. Basov, R. Hillenbrand, M. F. Craciun, F. J. García De Abajo, S. Russo, and F. H. L. Koppens, Nano Lett. **17**, 5908 (2017).
[61] T. Low, F. Guinea, H. Yan, F. Xia, and P. Avouris, Phys. Rev. Lett. **112**, 116801 (2014).
[62] H. Yan, T. Low, F. Xia, and P. Avouris, Nano Lett. **14**, 4581 (2014).
[63] Y. Jia, H. Zhao, Q. Guo, X. Wang, H. Wang, and F. Xia, ACS Photonics **2**, 907 (2015).
[64] S. Dai, Q. Ma, M. K. Liu, T. Andersen, Z. Fei, M. D. Goldflam, M. Wagner, K. Watanabe, T. Taniguchi, M. Thiemens, F. Keilmann, G. C. A. M. Janssen, S. E. Zhu, P. Jarillo-Herrero, M. M. Fogler, and D. N. Basov, Nat. Nanotechnol. **10**, 682 (2015).
[65] A. Principi, M. Carrega, M. B. Lundeberg, A. Woessner, F. H. L. Koppens, G. Vignale, and M. Polini, Phys. Rev. B **90**, 165408 (2014).
[66] H. Yan, T. Low, W. Zhu, Y. Wu, M. Freitag, X. Li, F. Guinea, P. Avouris, and F. Xia, Nat. Photonics **7**, 394 (2013).
[67] Y. Liu and R. F. Willis, Phys. Rev. B **81**, 081406(R) (2010).
[68] J. Schiefele, J. Pedrós, F. Sols, F. Calle, and F. Guinea, Phys. Rev. Lett. **111**, 237405 (2013).
[69] Z. Y. Ong and M. V. Fischetti, Phys. Rev. B **86**, 165422 (2012).
[70] M. J. Brahlek, N. Koirala, J. Liu, T. I. Yusufaly, M. Salehi, M. G. Han, Y. Zhu, D. Vanderbilt, and S. Oh, Phys. Rev. B **93**, 125416 (2016).
[71] T. Stauber, G. Gómez-Santos, and L. Brey, ACS Photonics **4**, 2978 (2017).
[72] N. Bansal, Y. S. Kim, M. Brahlek, E. Edrey, and S. Oh, Phys. Rev. Lett. **109**, 116804 (2012).
[73] L. Wu, W. K. Tse, M. Brahlek, C. M. Morris, R. V. Aguilar, N. Koirala, S. Oh, and N. P. Armitage, Phys. Rev. Lett. **115**, 217602 (2015).
[74] A. Y. Nikitin, F. Guinea, F. J. Garcia-Vidal, and L. Martin-Moreno, Phys. Rev. B **85**, 081405(R) (2012).
[75] J. Christensen, A. Manjavacas, S. Thongrattanasiri, F. H. L. Koppens, and F. J. García De Abajo, ACS Nano **6**, 431 (2012).
[76] J. H. Strait, P. Nene, W. M. Chan, C. Manolatou, S. Tiwari, F. Rana, J. W. Kevek, and P. L. McEuen, Phys. Rev. B **87**, 241410(R) (2013).
[77] A. Scholz, T. Stauber, and J. Schliemann, Phys. Rev. B **86**, 195424 (2012).
[78] N. Verellen, P. Van Dorpe, C. Huang, K. Lodewijks, G. A. E. Vandenbosch, L. Lagae, and V. V Moshchalkov, Nano Lett. **11**, 391 (2011).
[79] F. Hao, P. Nordlander, Y. Sonnefraud, P. Van Dorpe, and S. A. Maier, ACS Nano **3**, 643 (2009).
[80] N. Verellen, P. Van Dorpe, D. Vercruysse, A. E. Guy, and V. V Moshchalkov, Opt. Express **19**, 11034 (2011).
[81] C. S. R. Kaipa, A. B. Yakovlev, G. W. Hanson, Y. R. Padooru, F. Medina, and F. Mesa, Phys. Rev. B **85**, 245407 (2012).
[82] J. Igo, S. Zhou, Z. G. Yu, O. P. Amnuayphol, F. Zhao, and Y. Gu, J. Phys. Chem. C **122**, 22849 (2018).
[83] N. Balakrishnan, C. R. Staddon, E. F. Smith, J. Stec, D. Gay, G. W. Mudd, O. Makarovsky, Z. R. Kudrynskyi, Z. D. Kovalyuk, L. Eaves, A. Patanè, and P. H. Beton, 2D Mater. **3**, 025030 (2016).
[84] X. Tao and Y. Gu, Nano Lett. **13**, 3501 (2013).

[85] J. Wang, C. Fan, J. He, P. Ding, E. Liang, and Q. Xue, Opt. Express **21**, 2236 (2013).

[86] V. Giannini, Y. Francescato, H. Amrania, C. C. Phillips, and S. A. Maier, Nano Lett. **11**, 2835 (2011).

[87] C. In, S. Sim, B. Kim, H. Bae, H. Jung, W. Jang, M. Son, J. Moon, M. Salehi, S. Y. Seo, A. Soon, M. H. Ham, H. Lee, S. Oh, D. Kim, M. H. Jo, and H. Choi, Nano Lett. **18**, 734 (2018).

[88] M. Autore, H. Engelkamp, F. D'Apuzzo, A. Di Gaspare, P. Di Pietro, I. Lo Vecchio, M. Brahlek, N. Koirala, S. Oh, and S. Lupi, ACS Photonics **2**, 1231 (2015).

[89] P. Di Pietro, M. Ortolani, O. Limaj, A. Di Gaspare, V. Giliberti, F. Giorgianni, M. Brahlek, N. Bansal, N. Koirala, S. Oh, P. Calvani, and S. Lupi, J. Phys.: Condens. Matter **29**, 183002 (2017).